Research Square

Preprints are preliminary reports that have not undergone peer review.
They should not be considered conclusive, used to inform clinical practice,
or referenced by the media as validated information.

A generative framework for precise topology engineering of polymer networks

Ahmet Yildirim
Northwestern University
Akash Arora
Dow Chemical (United States)
Dongchan Ahn
Dow Chemical (United States)
Sinan Keten
s-keten@northwestern.edu

Northwestern University

Article

Keywords:

Posted Date: July 13th, 2026

DOI: https://doi.org/10.21203/rs.3.rs-9589195/v1

License: This work is licensed under a Creative Commons Attribution 4.0 International License.
Read Full License

Additional Declarations: No competing interests reported.

A generative framework for precise topology engineering of polymer networks

Ahmet Burak Yıldırım,[†] Akash Arora,[‡] Dongchan Ahn,[‡] and Sinan Keten[*,†,¶]

[†]*Department of Mechanical Engineering, Northwestern University, Evanston, IL, USA*

[‡]*The Dow Chemical Company, Midland, MI, USA*

[¶]*Department of Civil and Environmental Engineering, Northwestern University, Evanston, IL, USA*

E-mail: s-keten@northwestern.edu

Abstract

The mechanical performance of crosslinked polymer networks is typically predicted from the average crosslink density, yet topological heterogeneity of the crosslink functionality distribution $P(f)$ can produce vast differences in elasticity and fracture at fixed density. Existing kinetic and reaction-diffusion algorithms cannot prescribe $P(f)$ precisely, limiting systematic topological studies. We introduce a generative framework that maps abstract graph topologies into physically equilibrated molecular networks at arbitrary resolution. Atomistic simulations of PDMS and PMTFPS built on identical graph topologies reproduce chemical specificity, capturing the distinct glass transition temperatures driven by side-group sterics. A coarse-grained ensemble of over 300 architectures at fixed mean functionality but varied $P(f)$ reveals a state-dependent hierarchy of design drivers: brittle networks fail via local stress concentrations (high betweenness centrality), while tough networks are governed by cooperative load sharing (high eigenvector centrality). Topological order thus acts as an orthogonal design variable to crosslink density, enabling mechanical tuning without altering chemistry.

Introduction

Predicting the thermomechanical performance of crosslinked polymer networks remains a fundamental challenge in materials science. The inherent disorder of the amorphous state obscures the direct relationship between synthetic inputs (monomer chemistry, network architecture, and cure conditions) and macroscopic mechanical properties, creating a persistent structure-property gap.[1,2] In particular, the macroscopic response is often determined not by mean-field averages, but by the emergent network architecture established during curing.[3,4] Accurate characterization of the network state thus requires statistical descriptors that transcend simple averages. Specifically, while chain-length distributions ($P(N)$) dictate elasticity,[5] the coupled crosslink-functionality ($P(f)$) and topological defect distributions govern non-linear failure properties, including tensile toughness and ultimate tensile strength (UTS),[6–9] where bond rupture events are increasingly linked to shortest-path statistics and centrality metrics.[6,10,11]

Historically, the field has relied on metrics such as the average crosslink density ($\langle\nu\rangle$) to describe the network state. However, detailed structural analysis demonstrates that this metric proves insufficient for capturing the true topological structure.[12] Critically, networks with nominally identical $\langle\nu\rangle$ exhibit significant scatter in their mechanical response solely due to variations in defect topology and spatial heterogeneity.[13–17] The ongoing search for more robust descriptors, such as effective crosslink density, confirms the fundamental limitations of mean-field averages.[18]

Thus, establishing a rigorous structure-property relationship necessitates methods capable of direct, *a priori* control over the underlying network topology. Current algorithms for constructing initial network configurations for molecular dynamics (MD) simulations do not address this requirement. Distance-based methods and kinetic Monte Carlo schemes[19–22] simulate the crosslinking process directly. While physically intuitive, these approaches yield topology as an emergent, uncontrolled outcome rather than a design input,[23] a limitation that persists even in modern covalent adaptable networks where topology remains largely

stochastic.[24] Similarly, the current lattice-based approaches[25] offer deterministic control but retain the crystallographic signatures of the underlying grid. Related lattice-based Monte Carlo methods such as the Bond Fluctuation Model (BFM)[26–28] mitigate these crystallographic artifacts via variable-length bond moves but are designed to simulate polymer dynamics rather than to prescribe the network topology *a priori*.

We present a multi-scale computational framework that prescribes network topology *a priori*, decoupling it from the stochastic curing path. Unlike kinetic approaches, we model the network as an explicit graph object before chemical instantiation, conceptually inverting traditional methods that map melts to meshes.[29] This allows for the direct manipulation of topological variables, such as the variance of the crosslink functionality ($P(f)$), as independent input parameters, avoiding the finite-conversion drift that perturbs $P(f)$ in reaction-based schemes. Notably, the same graph-theoretical skeleton can be embedded in chemically distinct systems, a capability unavailable to kinetic methods where chemistry inevitably shapes topology. By bypassing the computational expense of reaction simulation, this method enables the rapid generation of extensive statistical ensembles. We exploit this capability to identify the specific graph-theoretical origins of the broad mechanical property distributions at constant mean degree, establishing network topology as a distinct, tunable dimension for the inverse design of soft materials.

We validate the physicochemical accuracy of the framework through atomistic MD simulations of polydimethylsiloxane (PDMS) and poly(methyl 3,3,3-trifluoropropylsiloxane) (PMTFPS) networks. Our analysis reveals that the steric hindrance of fluorinated side groups yields increased chain stiffness (scaling exponent $\nu \approx 0.48$) and elevated glass transition temperatures ($T_g \approx 200$ K) compared to PDMS, consistent with experimental expectations.[30,31] Additionally, the local chain statistics exhibit a Brownian bridge distribution, confirming the presence of topological constraints. Extending this analysis to coarse-grained ensembles, we demonstrate that fracture strength and toughness depend critically on graph-theoretical metrics rather than mean-field descriptors such as crosslink density or mean functionality. No-

tably, we observe that networks with high eigenvector centrality exhibit enhanced toughness, as cooperative load-sharing architectures prevent stress localization.

We begin by describing the graph generation and embedding algorithms. Following this, we validate the chemical fidelity of the framework through an analysis of local chain statistics and thermodynamic transitions in atomistic networks. Finally, we use the scalability of the model to generate ensembles of coarse-grained networks to isolate the graph-theoretical origins of property scatter, focusing on metrics such as centrality and assortativity.

Methods

To achieve systematic decoupling of topological architecture from chemical specificity, we employ a multi-stage computational framework. This approach deviates from traditional kinetic MD schemes, which simulate the temporal evolution of crosslinking reactions. While kinetic methods offer physical realism, they treat the final network topology as an emergent, uncontrolled outcome of the stochastic trajectory.[19,32–35] In contrast, we utilize a constructive graph-theoretical approach, enabling the direct, *a priori* prescription of the network's connectivity map. This strategy allows for the precise specification of statistical descriptors (e.g., the degree distribution $P(f)$ and cycle rank), facilitating the inverse design of material properties.[36]

Topological generation

The abstract network topology is generated using a novel constraint-satisfaction algorithm based on lattice pruning. The process is initialized by instantiating a fully connected precursor graph mapped onto a lattice scaffold (e.g., SC, BCC, or FCC) using only first-nearest-neighbor connectivity. The simulation domain dimensions (N_x, N_y, N_z) are independent, enabling the construction of non-cubic geometries essential for studying aspect-ratio-dependent phenomena in one- and two-dimensional systems, such as fibers and thin films. Furthermore, the

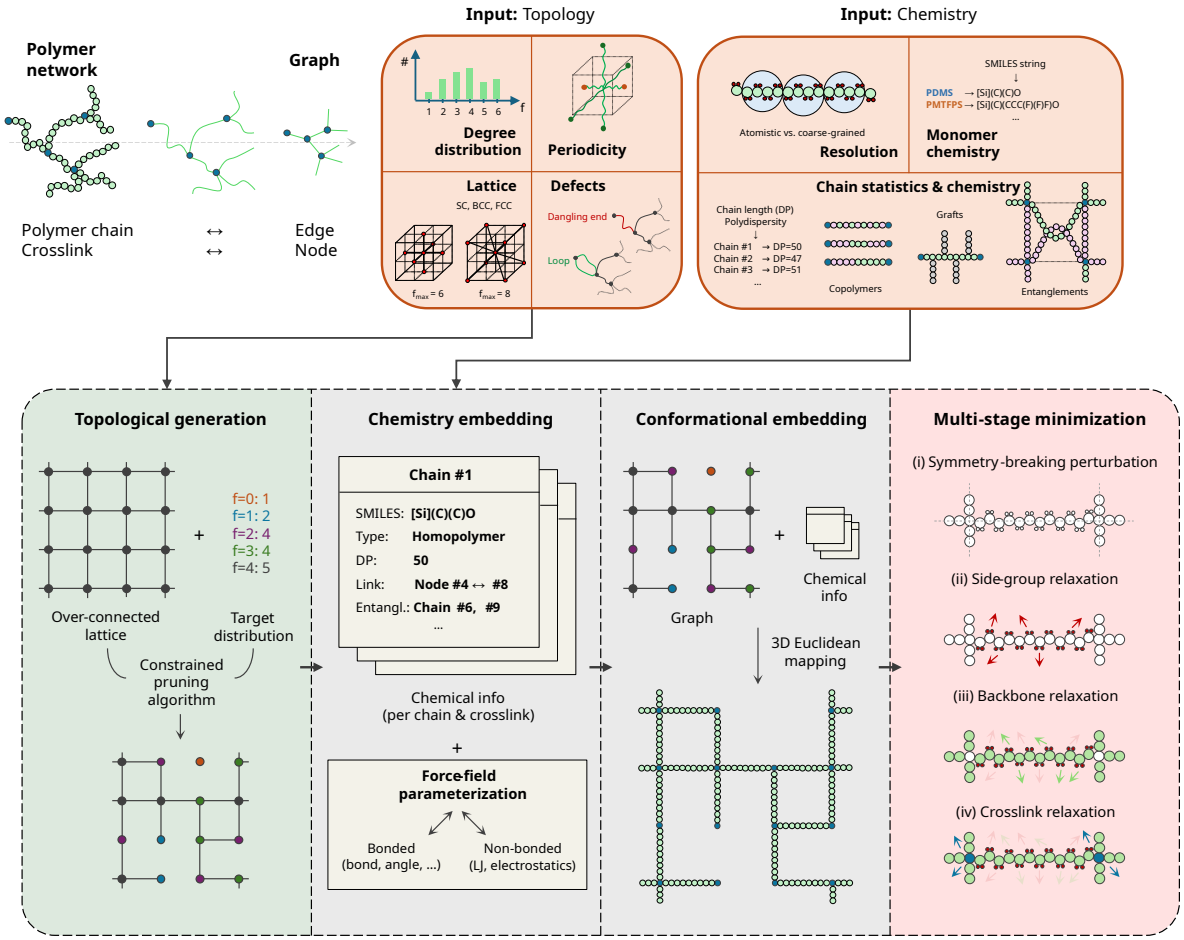


Figure 1: **Generative computational framework for topology-controlled polymer networks.** The workflow integrates abstract graph theory with physicochemical parameterization through a modular pipeline. **Input parameters** define the target architectural constraints (e.g., degree distribution, lattice periodicity) and chemical resolution (e.g., monomer SMILES, copolymer sequence, chain polydispersity). **Topological generation** employs a constrained subtractive pruning algorithm to carve a specific adjacency matrix from an over-connected lattice scaffold. **Chemistry embedding** instantiates each network chain as a discrete data object, assigning specific molecular identities and force-field parameters (bonded and non-bonded) to the topological edges. **Conformational embedding** maps the abstract graph into continuous 3D Euclidean space, translating connectivity into initial geometric coordinates. Finally, **Multistage minimization** executes a hierarchical relaxation protocol, comprising (i) symmetry-breaking perturbation, (ii) side-group relaxation, (iii) backbone relaxation, and (iv) crosslink relaxation, to resolve high-energy steric overlaps and generate a stable, clash-free configuration suitable for subsequent MD equilibration.

framework accommodates both fully periodic boundaries for bulk systems and partially aperiodic constraints, extending its applicability beyond standard isotropic melts. We

emphasize that this lattice serves strictly as a high-density search space to guarantee efficient monomer packing; it does not impose a structural template, and its crystallographic symmetry vanishes during the subsequent physicochemical embedding and equilibration.[37]

From this over-connected state ($f_{lattice} > f_{target}$), the target topology is sculpted via a hierarchical stochastic pruning process. Unlike random bond percolation, which typically yields uncontrolled, broad degree distributions dependent on a single probability parameter,[37] our novel algorithm removes edges iteratively to satisfy a complex, user-defined degree distribution $P(f)$ while strictly maintaining the Giant Connected Component (GCC),[38] consistent with the connectivity thresholds established for soft random geometric graphs.[39] However, we acknowledge that the realizability of a target $P(f)$ is non-trivial; not all mathematical distributions can be embedded within a Euclidean lattice due to geometric frustration and the constraints of the Handshake Lemma.[40,41] As the lattice size increases, the combinatorial search space expands, revealing a topological degeneracy where multiple distinct architectures can satisfy a single statistical target. Consequently, while $P(f)$ alone is an insufficient descriptor of network topology, this degeneracy provides a vast library for inverse design, allowing specific architectures to be filtered from the ensemble based on targeted graph metrics. These degenerate architectures are distinguished by higher-order descriptors (loop order, centrality measures, assortativity) defined in the Appendix, which we exploit in the Results section to dissect the mechanical scatter at fixed $\langle f \rangle$. The pruning is executed in three distinct stages. First, the algorithm performs a targeted introduction of defects, where nodes are randomly selected to act as unreacted sites ($f = 0$) or dangling ends ($f = 1$) until the specific target densities are met. Second, it enforces chemical realism by iteratively removing edges from any node exceeding the maximum valency (f_{max}) of the target monomer (e.g., $f_{max} = 4$ for silicon centers). Third, a Monte Carlo minimization loop targets the remaining edges to converge the global $P(f)$ distribution to the input specification. We omit bifunctional ($f = 2$) nodes by construction because they correspond to chain extensions rather than true branch points. Throughout this process, a Union-Find data structure

validates global connectivity before every deletion, ensuring the final graph represents a single, cohesive network free of isolated clusters. Following this generation phase, the workflow supports a supplementary modification step to introduce higher-order topological defects. By scanning the established graph for permissible node or edge configurations, the algorithm systematically inserts specific non-ideal motifs, such as primary loops and higher-order loops. Primary loops attach a chain to a single crosslink, while higher-order loops are generated by appending parallel chains between two already-connected nodes. These insertions are applied as a post-processing step that intentionally perturbs the raw degree distribution; loop-associated edges are tagged so that they can be distinguished from backbone edges in effective-degree analyses.

Chemical and conformational embedding

The translation of the abstract network into a physical model is performed via a deterministic embedding routine that separates connectivity from chemical identity. We employ a modular assignment routine to map molecular definitions to the graph elements. For atomistic models, the RDKit library[42] interprets monomeric SMILES strings to generate chemically detailed networks. The framework automates force-field parameterization by recursively traversing the graph topology to identify and assign all required angle, dihedral, and improper potentials based on local chemical environments (i.e., neighboring atom types) and hybridization states. This ensures that the complex connectivity of the network is fully physically described without the need for manual topology definition.

This framework accommodates diverse molecular architectures, including chain-length polydispersity, sequence-defined copolymers (e.g., alternating or blocky), and discrete mixtures of chemically distinct chains. Furthermore, the protocol enables the systematic incorporation of side-chain grafts, parameterized directly by their monomeric SMILES, degree of polymerization, and grafting density. Although we parameterize these systems using the DREIDING force field[43] in the present work, the underlying mapping algorithm is force-field agnostic, theo-

retically supporting the integration of arbitrary interaction potentials. Similarly, for mesoscale investigations, the framework utilizes the standard Kremer-Grest bead-spring formalism,[44] mapping bead types directly to topological features without algorithmic modification.

Geometric instantiation maps the lattice nodes into 3D Euclidean space. Each chain is instantiated as a sequence of beads placed equidistantly along the straight line connecting its two crosslink nodes (via the minimum-image displacement); the subsequent multi-stage relaxation resolves this artificial geometry. Unlike phantom network models, our approach explicitly accounts for topological constraints: we introduce inter-chain entanglements by modifying the embedding paths of two neighboring parallel chains so that they interweave, producing kinks consistent with a user-defined entanglement density.[45] Unlike kinetic simulations, where trapped entanglements emerge as a consequence of chain dynamics, our framework treats the entanglement density as a user-defined input, decoupled from chain length. Consequently, the entanglement molecular weight (N_e) can be prescribed independently of DP, enabling the controlled study of processing-dependent N_e variability at any chain length.[46] Additionally, the protocol supports the instantiation of volumetric crosslinks (e.g., POSS cages),[32] enabling the simulation of high-functionality junctions ($f \gg 4$) and rigid spatial constraints distinct from standard point-like nodes.

Multi-staged relaxation and equilibration

The initial embedding of chains via linear interpolation results in a geometrically accurate but energetically unfavorable state, characterized by significant atomic overlaps. Furthermore, the lattice-based origin of these coordinates creates artificial symmetries that can stall standard gradient-based minimization algorithms due to vanishing forces. To resolve these conflicts without inducing numerical instability, we implement a multi-stage relaxation protocol. First, we apply a symmetry-breaking geometric perturbation to avoid degenerate-force stalls in standard gradient-based minimization. This routine iteratively identifies hard steric clashes and applies small stochastic displacements to conflicting atoms, effectively resolving the most

severe overlaps and providing the directional bias required for subsequent energy minimization.

Following this geometric resolution, the process proceeds through a serial, soft-potential minimization in which successive groups of atoms are unfrozen in stages, starting with side groups, followed by chain backbones, and finally crosslink junctions (Fig. 1, steps ii–iv). This hierarchical unfreezing prevents the distortion of the topological skeleton while mitigating high-energy interactions.[19]

Subsequently, the system transitions to dynamic time integration using a force-limiting algorithm. This integration scheme permits the gradual ramping of non-bonded potentials from soft repulsive barriers to the full interaction potential, safely converting residual potential energy into kinetic motion. At this stage, the simulation is fully stable under standard force-field constraints, allowing for unrestricted molecular dynamics and user-defined equilibration protocols. For the material properties reported in this work, we employed a comprehensive thermal annealing cycle ($T \gg T_g$) to ensure the complete erasure of lattice correlations and the attainment of a relaxed, amorphous state.

Simulation details

For the atomistic networks reported here, we set the algorithmic entanglement density to zero, isolating the topology-driven response at chain lengths below the experimental N_e. Both PDMS and PMTFPS networks were generated from an identical $5 \times 5 \times 5$ simple-cubic lattice scaffold with fully periodic boundaries, with a prescribed degree distribution of 69 tetrafunctional, 46 trifunctional, 6 monofunctional nodes, and 4 vacancies ($\langle f \rangle \approx 3.5$, 210 chains). Three monodisperse strand lengths ($DP = 10, 30, 100$) were studied, producing systems of $\sim 2 \times 10^4$–3.4×10^5 atoms depending on chemistry and chain length. All systems were parameterized with the DREIDING force field[43] using Gasteiger charges, with non-bonded interactions treated via LJ/Coulomb potentials (10 Å cutoff) and PPPM electrostatics (10^{-4} accuracy). Following multi-stage energy minimization, thermal equilibration was performed with a 1 fs timestep using alternating NVT and NPT blocks (0.5 ns each) at each

temperature, stepping down from 1000 K to 400 K in 100 K decrements. NPT runs used an isotropic barostat at $P = 1$ atm with temperature and pressure damping constants of 100 fs and 1000 fs, respectively. The systems were then further equilibrated at 300 K for 25 ns under NPT conditions to ensure complete relaxation at ambient conditions.

For the coarse-grained fracture ensemble, we generated over 300 unique network architectures on a $6 \times 6 \times 6$ SC lattice (216 sites, 206 crosslinker nodes, ∼360 chains per realization) with average crosslink functionality $\langle f \rangle \approx 3.5$ (above the Flory gelation threshold of 3, enabling variation in $P(f)$ without approaching the gel point) and systematically varied degree distributions $P(f)$. Each system included exactly 10 degree-0 nodes (∼4.6% of nodes). These correspond to vacant lattice positions that contain no chain or crosslinker, introducing a small fraction of unreacted sites that contribute to amorphous packing; the count is not tied to a percolation threshold but was chosen pragmatically as a minimal perturbation held fixed across the ensemble for consistency. Networks were modeled using the Kremer-Grest bead-spring formalism[44] with monodisperse $DP = 30$ chains. Non-bonded interactions for all bead pairs used a standard LJ potential with $\epsilon = 1.0$, $\sigma = 1.0$, and an attractive cutoff $r_c = 2.5\sigma$ (yielding an equilibrium density $\rho \approx 0.89\sigma^{-3}$). During equilibration, bonded interactions were described by the standard FENE potential ($K = 30\epsilon/\sigma^2$, $R_0 = 1.5\sigma$). Systems were equilibrated via multi-stage annealing under NPT conditions ($\Delta t = 0.002\tau$): a warm-up ramp to $T = 1.7\epsilon/k_B$, a high-temperature soak (10^6 steps), stepwise cooling to $T = 1.0\epsilon/k_B$, and five extended production blocks (2×10^6 steps each), totaling approximately 1.4×10^7 steps. For the uniaxial tensile tests, the bond style was switched to a quartic potential ($K = 101.6\epsilon/\sigma^2$, $B_1 = 1.94\epsilon/\sigma$, $B_2 = -0.917\epsilon$, $R_c = 1.47\sigma$, $U_0 = 43.96\epsilon$) that permits irreversible covalent scission at the critical extension R_c.[15] Deformation was applied at a constant engineering strain rate $\dot{\epsilon} = 5 \times 10^{-4}\tau^{-1}$ ($\Delta t = 0.005\tau$) under NPT conditions with transverse pressure relaxation ($P = 0$), comparable to the protocol employed by Hagita et al.[15] Each network was deformed independently along three orthogonal axes to eliminate anisotropic artifacts. We note that the strain at break and toughness are strongly correlated

across the ensemble (Pearson $r = 0.94$), and we therefore report toughness as the primary extensibility descriptor, as it additionally captures the energy dissipation capacity of the network. Both UTS and toughness, extracted from the peak and integral of the stress–strain curve respectively, are robust to low-strain noise. The Young's modulus is not reported: its initial-slope estimate exhibited persistent finite-size fluctuations that were unchanged under slower strain rates, and reducing the noise would require enlarging each system (more beads per chain or a larger lattice), either of which would alter the controlled variables (DP or $P(f)$) that define this ensemble.

Results

The utility of any generative algorithm depends on its ability to reproduce physical properties consistent with experimental reality. In this section, we first assess the physicochemical fidelity of our framework using fully atomistic simulations. We focus on two silicone variants, PDMS and PMTFPS, which differ only in their side-group bulkiness. This comparison allows us to test if the generative framework respects the distinct spatial requirements and conformational statistics of different monomer chemistries. We specifically analyze the radial distribution functions and characteristic ratios to ensure the networks are amorphous and equilibrated.

Once the structural baseline is established, we shift our focus to the macroscopic mechanical response. Predicting stochastic failure properties, such as toughness, necessitates robust statistical sampling across diverse topological realizations. To achieve the necessary statistical power, we adopt a coarse-grained bead-spring representation for the fracture studies. This approach enables us to quantify the effect of topological descriptors on the stress-strain behavior, decoupling these geometric effects from the specific chemical identity of the chain backbone.

Structural characterization of atomistic networks

To validate the efficacy of our generative and relaxation framework in producing physically equilibrated amorphous networks, we perform a multiscale structural analysis. Figure 2a presents the radial distribution functions (RDF), $g(r)$, between crosslinking nodes in PDMS and PMTFPS networks with strand length $N = 30$, compared against the initial crystalline reference lattice. The reference exhibits sharp Bragg peaks at characteristic lattice spacings, while both networks show a complete absence of long-range order, with $g(r) \approx 1$ beyond the first coordination shell. This confirms that the relaxation protocol successfully eliminates structural correlations from the initial scaffold, yielding a homogeneous, amorphous network for both chemistries.

Local monomer packing is governed by chemistry rather than network architecture. Figure 2b displays the monomer–monomer RDF for PDMS across varying degrees of polymerization ($DP = 10, 30, 100$). The profiles overlap nearly exactly in the short-range regime ($r < 10$ Å), indicating that nearest-neighbor distances and local coordination are dictated by local bonded potentials and excluded volume, independent of strand length.

At the mesoscale, the conformation of network strands reveals how chemical modification interacts with topological constraints. Figure 3a presents the scaling of the mean-squared end-to-end distance $\langle R_{ee}^2 \rangle$ with degree of polymerization N, following $\langle R_{ee}^2 \rangle \sim N^{2\nu}$. For PDMS, we find $\nu \approx 0.43$, indicating a slight contraction relative to the ideal Gaussian chain ($\nu = 0.5$), reflecting the topological constraints imposed by crosslinking and by the surrounding network of chains, which restricts each strand to a tube-like set of accessible conformations.[47,48] In contrast, PMTFPS exhibits $\nu \approx 0.48$, approaching ideal scaling. As corroborated by the shift toward larger end-to-end distances in the $P(R_{ee})$ distributions (Figure 3b), this structural shift reflects the influence of bulky trifluoropropyl side groups, which combine increased steric bulk with the strong polarity of C–F bonds, together stiffening the local chain and counteracting this network-induced contraction. The corresponding end-to-end distance distributions $P(R_{ee})$ in Figure 3b verify this observation: PMTFPS

histograms tend to be shifted toward larger R_{ee} values compared to PDMS, though the difference is small for short chains ($DP = 10, 30$) and becomes clearly resolvable only at $DP = 100$. Both sets of distributions broaden systematically with increasing chain length.

Finally, we directly test whether the simulated strands obey the statistics of a crosslinked network. In a rubber, each strand is pinned at both ends by its crosslinks, forming a Brownian bridge whose conformational statistics differ from those of a free chain.[49] Figure 4 shows the characteristic ratio $C_n = \langle R^2(n)\rangle/(n\ell^2)$ as a function of sub-chain index n for PDMS and PMTFPS at $DP = 10, 30, 100$. For all systems, C_n rises to an apparent plateau at small n before decaying as n approaches the total strand length N (i.e., the degree of polymerization, DP). This decay is the signature of the bridge constraint, where the fixed chain ends suppress long-wavelength fluctuations, limiting the dimensions of large sub-chains.[49] The solid lines represent predictions from a semi-flexible Brownian bridge model. To construct this model, we first generate a large ensemble of discrete freely-rotating chains, where successive bond vectors are correlated through a fixed deflection angle θ satisfying $\cos\theta = (C_\infty - 1)/(C_\infty + 1)$. From this unconstrained ensemble, we then retain only configurations whose end-to-end distance matches the mean $\langle R_{ee}\rangle$ observed in the simulation, effectively enforcing the bridge constraint by rejection sampling. The only adjustable parameter, C_∞, is chosen to match the plateau region of the measured C_n. While the model captures the general behavior, the simulation data decays more sharply at large n. This discrepancy arises because the model treats each strand as non-interacting, allowing it to pass freely through all other strands without penalty. In the simulated networks, however, the surrounding chains are uncrossable, and their positions are permanently fixed by the global network connectivity. This physical confinement restricts each strand to a narrow, tube-like region of accessible configurations, suppressing its transverse fluctuations below this non-interacting prediction.[50]

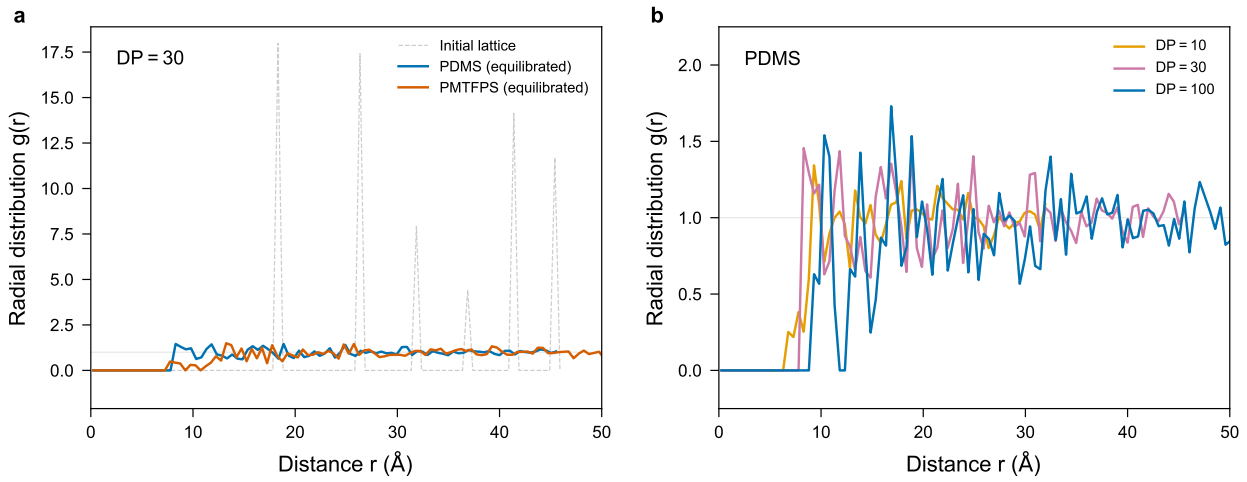


Figure 2: **Local structure and disappearance of lattice memory via equilibration.** (a) Radial distribution function $g(r)$ between crosslink nodes for PDMS and PMTFPS networks ($DP = 30$) compared to the crystalline reference. The absence of Bragg peaks confirms complete amorphization. (b) Monomer–monomer RDF for PDMS at different strand lengths. Local packing is independent of DP, indicating chemistry-driven short-range order.

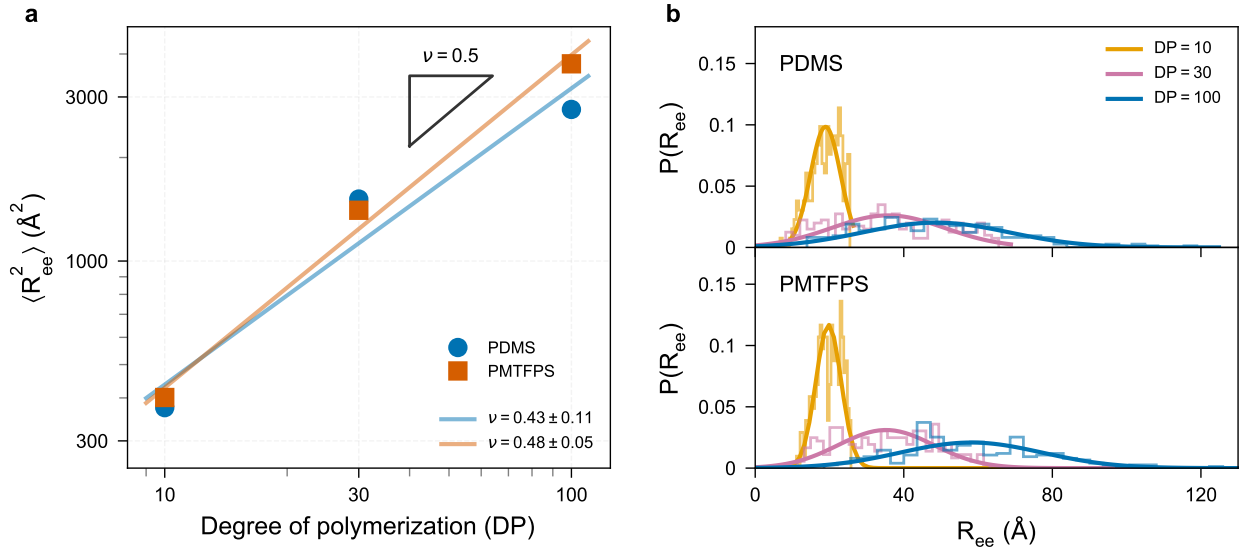


Figure 3: **Chain scaling and end-to-end distributions.** (a) Mean-squared end-to-end distance $\langle R_{ee}^2 \rangle$ versus degree of polymerization DP for PDMS ($\nu \approx 0.43$) and PMTFPS ($\nu \approx 0.48$). Triangle indicates ideal Gaussian scaling ($\nu = 0.5$). (b) Probability distributions $P(R)$ of the end-to-end distance for $DP = 10, 30, 100$. PMTFPS chains adopt more extended conformations than PDMS at the same DP.

Thermodynamic validation

To assess the framework's ability to capture chemical specificity beyond static structure, we characterize the glass transition temperature (T_g) of the equilibrated networks. We determine

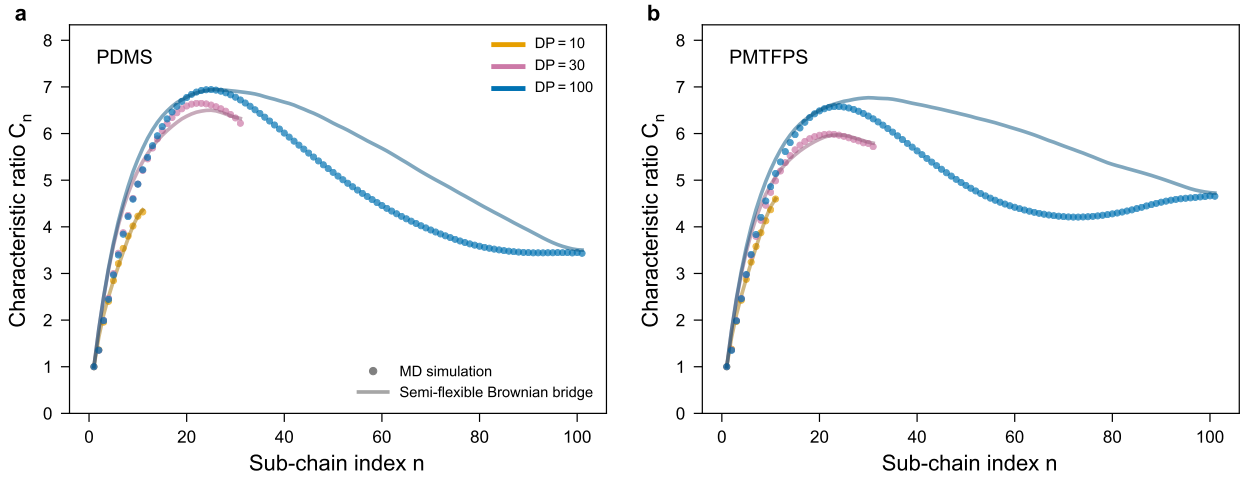


Figure 4: **Brownian bridge statistics of network strands.** Characteristic ratio C_n as a function of sub-chain index n for (a) PDMS and (b) PMTFPS networks. Simulation data (symbols) show the characteristic decay as $n \to N$, in qualitative agreement with the theoretical semi-flexible Brownian-bridge model (gray solid lines). This confirms that strands are topologically pinned at crosslinks, validating the network's entropic elasticity.

T_g using a stepwise cooling protocol, sweeping from 310 K down to 100 K in 5 K decrements. At each temperature step, the system is equilibrated for 0.2 ns before data collection. We monitor the mean-squared displacement (MSD) of network atoms over a fixed short interval ($t = 4$ ps) to probe local segmental mobility. To reduce statistical noise, we report the average MSD calculated from five independent short trajectories at each temperature. We quantify T_g by fitting the temperature-dependent MSD data to a continuous piecewise bilinear function, defining the transition temperature as the intersection point between the vibrational (glassy) and mobile (rubbery) regimes.

Figure 5 compares the thermal response for PDMS and PMTFPS networks instantiated from identical graph topologies. For PDMS, we obtain $T_g \approx 152$ K. This value aligns well with experimental benchmarks for crosslinked PDMS elastomers, which report transitions in the 146–154 K range depending on formulation.[51] For PMTFPS, we observe a substantial increase to $T_g \approx 193$ K. This result is consistent with the experimental value of ≈ 203 K (-70°C) reported for fluorinated polysiloxanes.[52] These transition temperatures show minimal variation across different chain lengths ($DP = 10$ to 100), indicating that in these densely

crosslinked networks, the glass transition is governed mainly by local segmental dynamics rather than global topology.

The observed ~ 40 K increase in T_g is a direct consequence of the distinct physicochemical properties of the trifluoropropyl side groups.[52] Substitution of the fluorinated moiety for one of the methyl groups on each Si atom introduces three key effects: (1) the higher atomic mass of fluorine atoms slows down segmental motion; (2) the strong C–F dipole moments increase intermolecular friction; and (3) the bulkier side groups introduce steric hindrance that suppresses backbone rotational freedom. Together, these factors significantly suppress local segmental mobility, raising the energy barrier for the onset of rubbery behavior. This ability to quantitatively reproduce both the absolute T_g values and the magnitude of their difference confirms that the force-field embedding and relaxation procedures successfully translate abstract chemical motifs into realistic, chemistry-specific dynamic behavior.

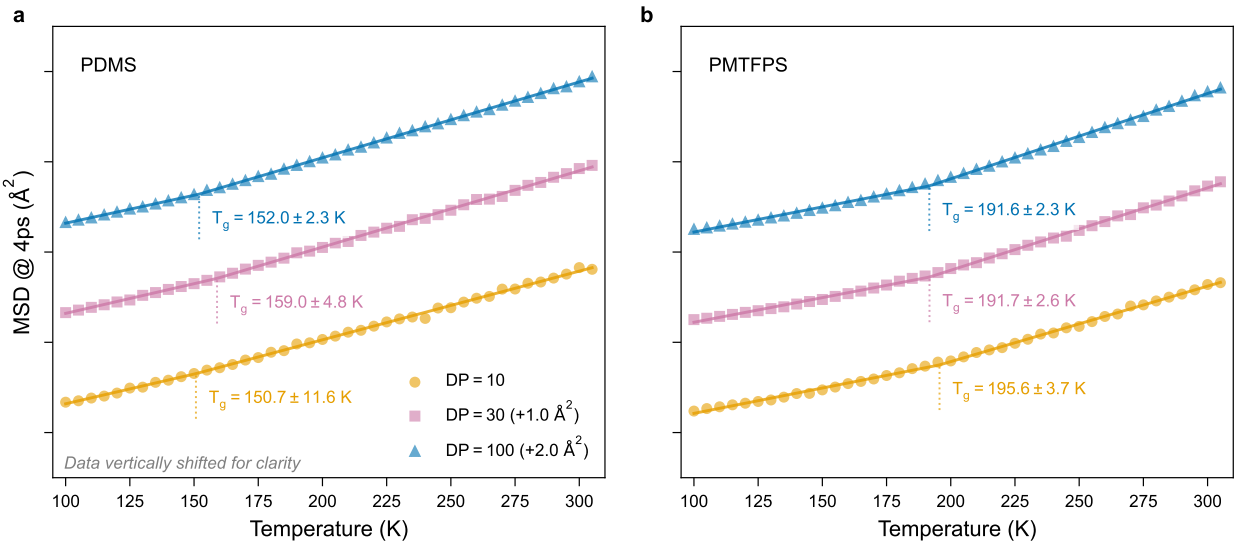


Figure 5: **Dynamic glass transition analysis.** Atomic mean-squared displacement (MSD) at 4 ps as a function of temperature for (a) PDMS and (b) PMTFPS networks. The intersection of linear fits to the glassy and rubbery regimes defines T_g. PMTFPS displays a significantly higher T_g (~ 193 K) compared to PDMS (~ 152 K) due to the steric hindrance of fluorinated side groups. Data series for different DP are vertically shifted for clarity; the transition temperature remains largely independent of strand length.

Data-driven topological mapping

To isolate the topological origins of mechanical failure, we generated an ensemble of over 300 unique network architectures with constrained average connectivity $\langle f \rangle \approx 3.5$ but systematically varied degree distributions $P(f)$. Figure 6a maps the mechanical performance of the ensemble. Despite identical average crosslink densities, the networks exhibit a wide dispersion in ultimate tensile strength (UTS) and toughness (energy to break). We partition this domain into four quadrants based on median performance thresholds: Weak/Brittle (Q1), Weak/Tough (Q2), Strong/Brittle (Q3), and Strong/Tough (Q4). Analyzing the crosslink functionality distributions $P(f)$ for these groups reveals a clear structural signature (Figure 6b). Low-performance networks (Q1) exhibit broad distributions with a disproportionate fraction of high-functionality nodes ($f = 5, 6$). This skew indicates that brittle failure is driven by the presence of dense, high-degree clusters, which likely act as local stress concentrators.[7,53–55] Notably, the transition to the intermediate toughness regime (Q2) coincides with a reduction in these high-functionality crosslinkers ($f = 6$) and the emergence of a bimodal distribution (peaks at $f = 3$ and 5). This suggests that while removing the most severe outliers enhances toughness, the resulting structural segregation into high- and low-connectivity domains prevents the material from achieving high strength. Conversely, high-performance networks (Q4) display a sharp, unimodal concentration of connectivity around the mean ($f = 3, 4$). This confirms that structural homogeneity is a prerequisite for mechanical synergy; eliminating both outliers and bimodality in favor of a uniform distribution minimizes weak links and maximizes cooperative load-bearing, consistent with the enhanced yield strength observed in homogeneously crosslinked elastomers.[7,56]

To quantify which topological features drive the transition between these mechanical states, we calculated the standardized effect size (Cohen's d) for various graph metrics. This statistic measures the difference in means between two groups normalized by their pooled standard deviation; values of $|d| > 0.5$ and $|d| > 0.8$ are typically considered medium and large effects, respectively. Figure 7a presents a heatmap of these drivers. We observe that

the global stiffness (λ_2) acts as a universal promoter of mechanical integrity. We distinguish here between the standard algebraic connectivity (λ_2) and the backbone stiffness ($\lambda_{2,core}$). The latter is calculated on the graph's k-core (where $k \geq 2$), obtained by recursively pruning dangling ends ($f = 1$ nodes) until convergence. While $\lambda_{2,core}$ isolates the connectivity of the load-bearing skeleton, our analysis reveals that the standard λ_2 is the significantly stronger predictor of performance (Total $d = 1.4$ vs. 0.4). This dominance suggests that peripheral dangling ends, often treated as trivial, actively degrade the network's global stability; thus, a metric sensitive to the entire topology (λ_2) captures the true mechanical state better than one focused solely on the backbone. We speculate that, although the dangling-end fraction is similar across the ensemble, variations in their placement contribute to the λ_2 signal; this contribution is removed by the $\lambda_{2,core}$ pruning. Physically, λ_2 maps onto the graph's resistance to partitioning under edge removal, which we interpret as the full-topology collective resistance to global failure pathways.

However, other drivers are highly state-dependent. For initially brittle materials (Q1), the primary improvement mechanism is the elimination of local bottlenecks such as bridges and stress-concentrating nodes (Figure 7b). We quantify stress concentrations using maximum betweenness centrality, which identifies nodes that serve as bridges for many shortest paths. High betweenness implies a bottleneck where force lines converge, serving as primary loci for bond rupture events,[11,57] as confirmed by recent shortest-path fracture topology analysis.[10] Once the network achieves a baseline level of connectivity (Q3), the optimization strategy shifts. Further toughening is driven by metrics associated with global load sharing, specifically average eigenvector centrality. Unlike degree centrality (which counts neighbors), eigenvector centrality assigns high scores to nodes connected to other highly connected nodes. This metric identifies *shortcuts* for stress propagation, allowing the network to delocalize energy dissipation across a larger volume effectively.[58] This hierarchy implies that mechanical optimization requires a sequential strategy, prioritizing the elimination of fatal defects to ensure connectivity before maximizing topological order to facilitate stress delocalization.

While backbone connectivity and centrality metrics emerge as primary drivers, it is instructive to examine topological features that exerted minimal influence within this specific design space. Notably, loop density (cycle rank) exhibits a negligible effect size ($|d| < 0.1$) across the transitions in our heatmap, consistent with theoretical predictions for phantom networks where loops of order ≥ 3 are elastically neutral (i.e., contribute negligibly to the modulus),[59] though their effect on fracture properties remains less well established. However, previous studies have demonstrated that primary loops (order < 2) can significantly affect fracture properties, with increases in primary-loop concentration transforming low-toughness materials into high-toughness ones.[7,60] We attribute the negligible effect observed here to the constraints of our generative algorithm, which fixes the average crosslink functionality at $\langle f \rangle \approx 3.5$ with primary-loop populations in the low-fraction regime (typically $< 5\%$ in high-density networks[61]), thereby implicitly keeping the variance in loop statistics low relative to the broader variations in connectivity patterns. This suggests that while loops are critical in systems with variable density, in highly crosslinked, density-constrained networks, the global arrangement of the backbone ($\lambda_{2,core}$) becomes the dominant predictor of failure. This dominance of global connectivity over local loop statistics implies that for high-density resins, mechanical toughness depends less on specific local motifs and more on the uniformity of the stress-bearing skeleton.

Discussion

In this work, we established a computational framework for the bottom-up design of polymer networks, bridging the gap between abstract graph theory and physical material properties. By implementing a constrained pruning algorithm followed by a multi-stage relaxation protocol, we demonstrated that lattice-based topologies can be mapped into continuous Euclidean space without retaining crystallographic artifacts. The modular nature of this workflow establishes a foundation for generating diverse architectures beyond the specific

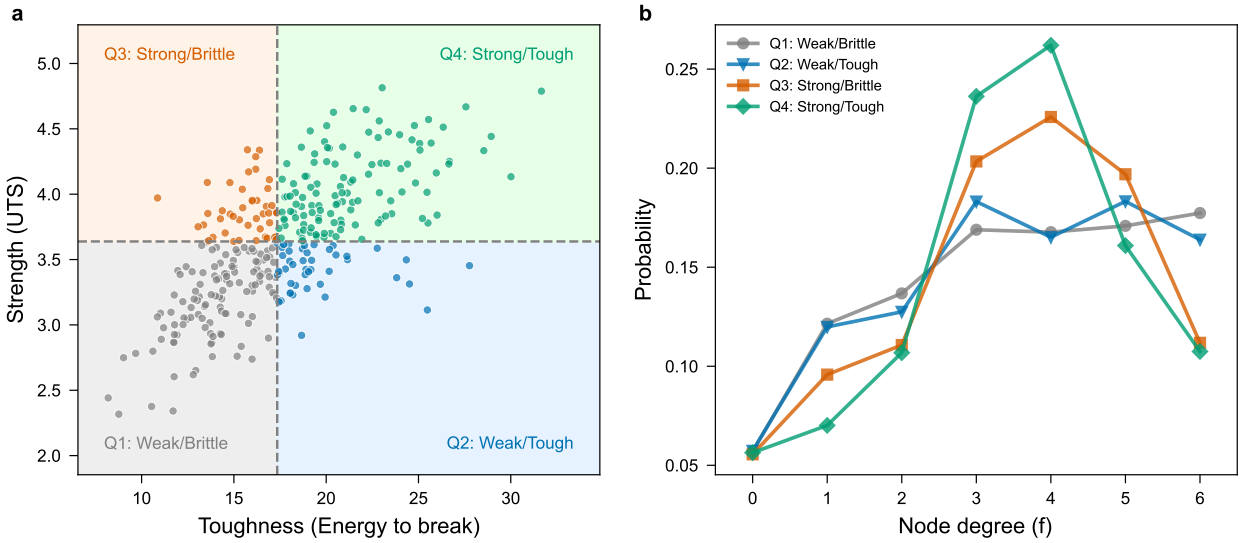


Figure 6: **Topological signatures of the strength-toughness synergy.** (a) Mechanical performance map of 300 coarse-grained networks with identical average connectivity ($\langle f \rangle \approx 3.5$). The design space is partitioned into four quadrants (Q1–Q4) based on median Strength and Toughness. (b) Node degree distributions $P(f)$ for each quadrant. High-performance Strong/Tough networks (Q4, green) exhibit a unimodal, homogenized distribution, whereas Weak/Brittle networks (Q1, gray) display significant structural heterogeneity.

systems analyzed here; the framework is readily extensible to polydisperse chain distributions, sequence-defined copolymers,[62] and entanglement constraints, while offering a pathway for modeling heterogeneous composite phases containing rigid-body inclusions (e.g., POSS nanocages or nanoparticles).[32,63,64]

We validated the physicochemical fidelity of this approach through atomistic molecular dynamics of silicone elastomers. Structural analysis verified that the relaxation process erases the initial lattice memory, yielding isotropic radial distribution functions and chain conformations consistent with Brownian bridge statistics. Furthermore, thermodynamic characterization confirmed that the embedding routine preserves chemical specificity. Despite sharing identical graph topologies, PMTFPS networks exhibited a glass transition temperature approximately 40 K higher than their PDMS counterparts ($T_g \approx 193$ K vs. 152 K). This shift accurately reflects the increased steric hindrance and dipole interactions of fluorinated side groups, proving that the generative algorithm captures local segmental dynamics independent of the global connectivity.

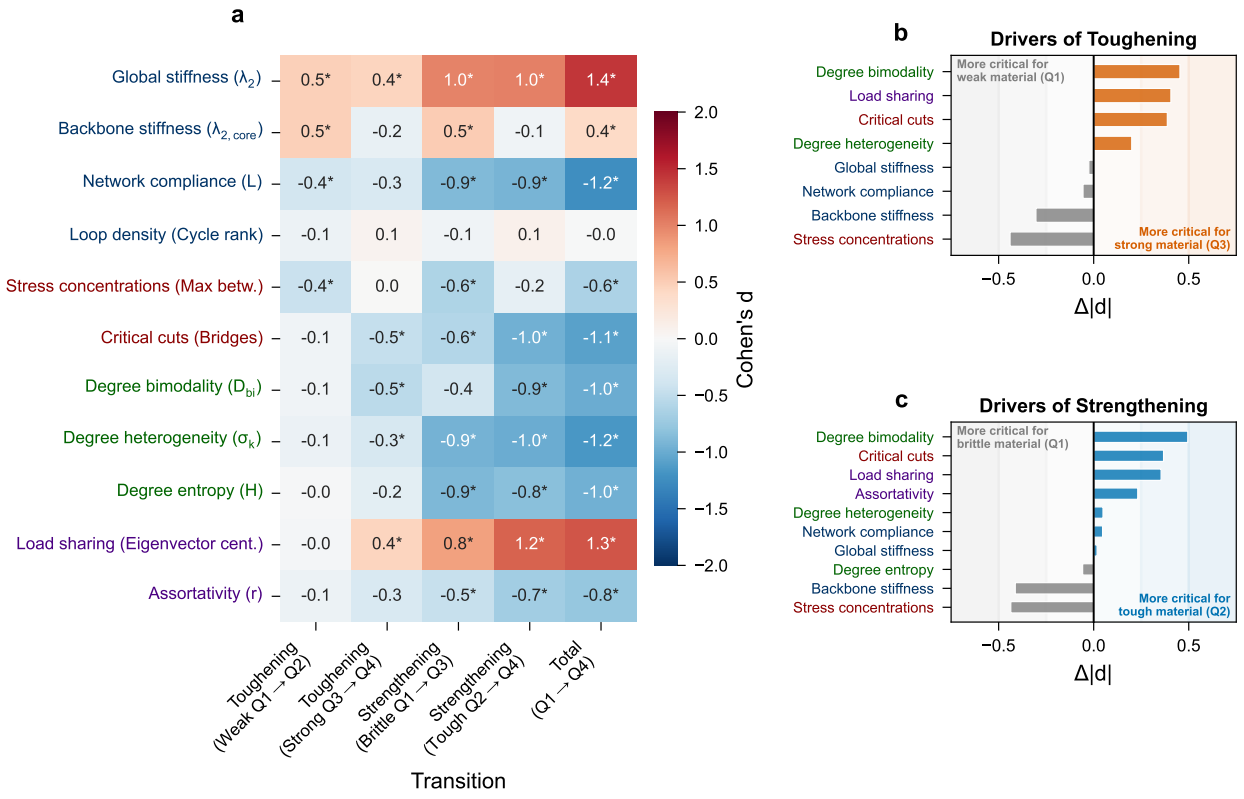


Figure 7: **State-dependent topological drivers.** (a) Heatmap of Cohen's d effect sizes quantifying the impact of topological features on mechanical transitions. Red indicates a positive driver; blue indicates a penalty. (b) Hierarchy of toughening mechanisms. For weak materials (Q1), toughness is limited by local defects (Stress Concentrations). For strong materials (Q3), toughening is driven by global connectivity (Load Sharing). (c) Hierarchy of strengthening mechanisms, showing a similar shift from defect-sensitivity to topology-dependence.

Extending this analysis to the mesoscale, we utilized coarse-grained simulations to isolate the impact of network architecture on mechanical failure. By testing an ensemble of over 300 distinct topologies at fixed mean functionality ($\langle f \rangle \approx 3.5$), we observed a significant dispersion in toughness and ultimate strength. Our analysis identified a state-dependent hierarchy of topological drivers. For brittle networks, mechanical performance is limited by local defects, specifically stress concentrations quantified by high betweenness centrality. In contrast, tough networks are governed by global connectivity metrics, such as eigenvector centrality, which facilitate cooperative load sharing. This transition highlights that optimizing a material requires different topological strategies depending on its baseline connectivity.

Finally, these results reveal that degree-distribution heterogeneity acts as an additional axis beyond crosslink density, which is the primary variable considered in classical rubber elasticity theory.[65] By holding both $\langle f \rangle$ and ν constant, we demonstrated that ultimate properties still vary significantly purely due to architectural heterogeneity. This decoupling suggests that topological design offers an orthogonal axis for material optimization, validating the distinction between density-driven elasticity and topology-driven failure established in model networks,[4] while further allowing for the tuning of fracture mechanics without altering the fundamental chemical composition. This capability suggests a pathway for future materials design,[66] where specific graph motifs are targeted to achieve distinct mechanical outcomes using chemically identical base subunits, or conversely, or conversely, where monomer choice is explored systematically within a fixed topology.

Acknowledgements

S.K. and A.B.Y. acknowledge funding from Dow Chemical Company through the collaborative UPI program, as well as support from the Department of Mechanical Engineering at Northwestern University. We also thank the Northwestern University High Performance Computing Center for providing a supercomputing grant.

Data Availability

The simulation data and analysis datasets generated during this study are available on Zenodo at `https://doi.org/10.5281/zenodo.19672939`.

Code availability

The generative framework (`topon`: TOpological POlymer Networks) and all analysis scripts used in this study are publicly available at `https://github.com/keten-group/topon`. The

repository includes the graph generation algorithm, chemical embedding routines, and the LAMMPS input scripts.

Author contributions

A.B.Y. developed the computational framework, performed the simulations, and analyzed the data. A.A. and D.A. helped define the research problem and motivation, contributed to the methodology, and provided technical guidance. S.K. supervised the project, secured funding, and provided overall direction. All authors discussed the results and contributed to writing the manuscript.

Competing interests

The authors declare no competing interests.

Appendix: Definition of topological metrics

To quantify the structural architecture of the generated polymer networks, we use a set of eleven graph-theoretical descriptors derived from the adjacency and Laplacian matrices, consistent with emerging graph-based frameworks for condensed matter systems.[67] The first family of metrics characterizes the global connectivity and spectral rigidity of the network. We define the global stiffness (λ_2) as the second smallest eigenvalue of the graph Laplacian, known as the algebraic connectivity. This value scales with the number of edges that must be cut to partition the graph, serving as a proxy for the overall mechanical resistance of the network. To isolate the load-bearing skeleton, we calculate the backbone stiffness ($\lambda_{2,core}$), defined as the algebraic connectivity of the 2-core subgraph obtained by recursively pruning dangling ends. In our ensemble, where $f = 2$ nodes are excluded by construction, this pruning removes only $f = 1$ dangling ends; any loops attached to $f \geq 3$ crosslinkers are

retained in the 2-core. We also evaluate compactness using the average shortest path length, the mean number of hops between any pair of nodes, where a lower value indicates a more compact topology. Finally, we calculate the loop density (cycle rank), which counts the number of fundamental independent cycles in the graph ($M - N + 1$). This metric quantifies the abundance of topological loops that govern chain extensibility and entropic elasticity.

The second group of descriptors identifies local defects and bottlenecks that limit mechanical performance. We compute the stress concentrations using maximum betweenness centrality, which identifies the node carrying the highest fraction of shortest paths. In a physical network, such nodes represent locations where force lines converge, creating likely initiation sites for fracture. We also determine the critical cuts (bridges), defined as the fraction of edges whose removal would disconnect the network. This metric quantifies the structural vulnerability, representing the density of single bonds solely responsible for maintaining global connectivity.

The third family focuses on the statistical distribution of node connectivity (degree), characterizing the homogeneity of the crosslinking. We calculate the degree bimodality (D_{bi}) using the bimodality coefficient, $D_{bi} = (\gamma^2 + 1)/\kappa$, where γ is the skewness and κ is the Pearson kurtosis of the degree sequence. Values of $D_{bi} > 5/9$ suggest a bimodal distribution, indicating the presence of structurally segregated populations of high-degree and low-degree nodes. We also measure the degree heterogeneity (κ_f), defined as the ratio of the second moment to the first moment of the degree distribution, $\kappa_f = \langle f^2 \rangle / \langle f \rangle$. For a perfectly homogeneous network where all nodes share the same degree, $\kappa_f = \langle f \rangle$, so deviations above this baseline quantify the breadth of the connectivity spread. Additionally, we compute the degree entropy (H) using the Shannon formulation, $H = -\sum_i p_i \ln p_i$, where p_i is the fraction of nodes with degree i. This metric measures the information content of the degree distribution, where higher entropy corresponds to a more randomized crosslinking pattern and lower entropy indicates a more ordered, concentrated distribution.

The final set of metrics captures higher-order correlations and cooperative mechanisms

within the topology. We use the load sharing metric, defined as the average eigenvector centrality, to measure the extent to which nodes are connected to other highly connected nodes. Unlike simple degree centrality, this recursive definition identifies shortcuts that facilitate stress delocalization across a large volume. Lastly, we calculate the assortativity coefficient (r), the Pearson correlation between the degrees of connected nodes.[68] Positive assortativity indicates a topology in which high-degree nodes tend to be connected to each other, while negative assortativity indicates mixing, where high-degree sites tend to be connected to low-degree neighbors.

References

(1) Gooneie, A.; Schuschnigg, S.; Holzer, C. A Review of Multiscale Computational Methods in Polymeric Materials. *Polymers* **2017**, *9*, 16.

(2) Barszczewska-Rybarek, I. A Guide through the Dental Dimethacrylate Polymer Network Structural Characterization and Interpretation of Physico-Mechanical Properties. *Materials* **2019**, *12*, 4057.

(3) Shundo, A.; Yamamoto, S.; Tanaka, K. Network Formation and Physical Properties of Epoxy Resins for Future Practical Applications. *JACS Au* **2022**, *2*, 1522–1542.

(4) Elder, R. M.; Sirk, T. W. Topological structure and mechanics of glassy polymer networks. *Soft Matter* **2017**, *13*, 8392–8401.

(5) Sorichetti, V.; Ninarello, A.; Ruiz-Franco, J.; Hugouvieux, V.; Kob, W.; Zaccarelli, E.; Rovigatti, L. Effect of Chain Polydispersity on the Elasticity of Disordered Polymer Networks. *Macromolecules* **2021**, *54*, 3769–3779.

(6) Vernerey, F. J.; Brighenti, R.; Long, R.; Shen, T. Statistical Damage Mechanics of Polymer Networks. *Macromolecules* **2018**, *51*, 6609–6622.

(7) Arora, A.; Lin, T.-S.; Olsen, B. D. Coarse-Grained Simulations for Fracture of Polymer Networks: Stress Versus Topological Inhomogeneities. *Macromolecules* **2022**, *55*, 4–14.

(8) Li, Y.; Dong, Z.; Li, M.; Huang, R.; Zhang, X.; Qian, H.; Lu, Z. Positional Isomerism Controls Epoxy Network Mechanics: Meta-Substitution Enhances Toughness via Adaptive Loop Dynamics from Multiscale Simulations. *ACS Macro Letters* **2025**, *14*, 1602–1608.

(9) Dookhith, A. Z.; Zhang, Z.; Ganesan, V.; Sanoja, G. E. Designing soft and tough multiple-network elastomers: impact of reversible radical deactivation on filler network architecture and fracture toughness. *Soft Matter* **2025**, *21*, 4029–4042.

(10) Yu, Z.; Jackson, N. E. Shortest Paths Govern Bond Rupture in Thermoset Networks. *Macromolecules* **2025**, *58*, 1728–1736.

(11) Zhang, H.; Riggleman, R. A. Predicting failure locations in model end-linked polymer networks. *Physical Review Materials* **2024**, *8*, 035604.

(12) Dobrynin, A. V.; Tian, Y.; Jacobs, M.; Nikitina, E.; Ivanov, D. A.; Maw, M.; Vashahi, F.; Sheiko, S. S. Forensics of polymer networks. *Nature Materials* **2023**, *22*, 1394–1400.

(13) Zhang, S.; Xi, L. Effects of Precursor Topology on Polymer Networks Simulated with Molecular Dynamics. *Polymer* **2017**, *116*, 143–152.

(14) Shen, J.; Lin, X.; Liu, J. Effects of Cross-Link Density and Distribution on Static and Dynamic Properties of Chemically Cross-Linked Polymers. *Macromolecules* **2019**,

(15) Hagita, K.; Murashima, T. Critical Importance of Both Bond Breakage and Network Heterogeneity in Hysteresis Loop on Stress–Strain Curves and Scattering Patterns. *Macromolecules* **2024**, *57*.

(16) Arora, A. Effect of Spatial Heterogeneity on the Elasticity and Fracture of Polymer Networks. *Macromolecules* **2025**, *58*, 1143–1155.

(17) Argun, B. R.; Statt, A. Interplay of Spatial and Topological Defects in Polymer Networks. *ACS Engineering Au* **2024**, *4*, 351–358.

(18) Gooranorimi, A.; Mousavifard, S.; Mohseni, M.; Yahyaei, H.; Makki, H. Effective Cross-Link Density as a Metric for Structure-Property Relationships in Complex Polymer Networks: Insights from Acrylic Melamine Systems. *ACS Applied Polymer Materials* **2025**, *7*, 9034–9044.

(19) Varshney, V.; Patnaik, S. S.; Roy, A. K.; Farmer, B. L. A Molecular Dynamics Study of Epoxy-Based Networks: Cross-Linking Procedure and Prediction of Molecular and Material Properties. *Macromolecules* **2008**, *41*, 6837–6842.

(20) Sirk, T. W.; Sliozberg, Y. R.; Brennan, J. K.; Lisal, M.; Andzelm, J. W. An enhanced entangled polymer model for dissipative particle dynamics. *The Journal of Chemical Physics* **2012**, *136*, 134903.

(21) Gissinger, J. R.; Jensen, B. D.; Wise, K. E. REACTER: A heuristic method for reactive molecular dynamics. *Macromolecules* **2020**, *53*, 9953–9961.

(22) Wang, R.; Lin, T.-S.; Johnson, J. A.; Olsen, B. D. Kinetic Monte Carlo Simulation for Quantification of the Gel Point of Polymer Networks. *ACS Macro Letters* **2017**, *6*, 1414–1419.

(23) Lang, M.; M
üller, T. Analysis of the Gel Point of Polymer Model Networks by Computer Simulations. *Macromolecules* **2020**, *53*, 498–512.

(24) Hafner, B. R.; Pal, S.; Lewis, B.; Keten, S.; Shull, K. R. Network Topology and Percolation in Model Covalent Adaptable Networks. *ACS Macro Letters* **2024**, *13*, 1545–1550.

(25) Tito, N. B.; Storm, C.; Ellenbroek, W. G. Self-Consistent Field Lattice Model for Polymer Networks. *Macromolecules* **2017**, *50*, 9788–9795.

(26) Carmesin, I.; Kremer, K. The Bond Fluctuation Method: A New Effective Algorithm for the Dynamics of Polymers in All Spatial Dimensions. *Macromolecules* **1988**, *21*, 2819–2823.

(27) Lang, M. Relation between Cross-Link Fluctuations and Elasticity in Entangled Polymer Networks. *Macromolecules* **2017**, *50*, 2547–2555.

(28) Nedelcu, S.; Werner, M.; Lang, M.; Sommer, J.-U. GPU implementations of the bond fluctuation model. *Journal of Computational Physics* **2012**, *231*, 2811–2824.

(29) Svaneborg, C. Inverse Primitive Path Analysis. *Computer Physics Communications* **2024**, *300*, 109209.

(30) Buch, R. R.; Klimisch, H. M.; Johannson, O. K. Light scattering and intrinsic viscosity investigation of polymethyl-3,3,3-trifluoropropylsiloxamer. *Journal of Polymer Science Part A-2: Polymer Physics* **1969**, *7*, 563–574.

(31) Kobayashi, H.; Nishiumi, W. Preparation and characterization of poly(methyl-3,3,3-trifluoropropylsiloxane-co-dimethylsiloxane). *Macromolecular Chemistry and Physics* **1993**, *194*, 1403–1410.

(32) Karnes, J. J.; Weisgraber, T. H.; Oakdale, J. S.; Mettry, M.; Shusteff, M.; Biener, J. On the Network Topology of Crosslinked Acrylate Photopolymers: A Molecular Dynamics Case Study. *The Journal of Physical Chemistry B* **2020**, *124*, 8473–8483.

(33) Jang, C.; Sirk, T.; Andzelm, J.; Abrams, C. Comparison of Crosslinking Algorithms in Molecular Dynamics Simulation of Thermosetting Polymers. *Macromolecular Theory and Simulations* **2015**, *24*, 260–270.

(34) Beech, H. K.; Wang, S.; Sen, D.; Rota, D.; Kouznetsova, T.; Arora, A.; Rubinstein, M.; Craig, S. L.; Olsen, B. D. Reactivity-Guided Depercolation Processes Determine Fracture Behavior in End-Linked Polymer Networks. *ACS Macro Letters* **2023**, *12*, 1685–1691.

(35) Li, J.; Zhang, K.; Tian, F.; Lei, X.; Shi, X.; Wang, J. Inherent Tensile Strength and Stretchability of Unentangled Elastomers. *Macromolecules* **2025**, *58*, 11445–11464.

(36) De Keer, L.; Cavalli, F.; Estupiñán, D.; Krüger, A.; Rocha, S.; Van Steenberge, P. H. M.; Reyniers, M.-F.; De Laporte, L.; Hofkens, J.; Barner, L.; D'hooge, D. R. Synergy of Advanced Experimental and Modeling Tools to Underpin the Synthesis of Static Step-Growth-Based Networks Involving Polymeric Precursor Building Blocks. *Macromolecules* **2021**, *54*.

(37) Torres-Knoop, A.; Schamboeck, V.; Govindarajan, N.; Iedema, P. D.; Kryven, I. Effect of different monomer precursors with identical functionality on the properties of the polymer network. *Communications Materials* **2021**, *2*.

(38) Puhlmann, P.; Zahn, D. Molecular Mechanisms of Silicone Network Formation: Bridging Scales from Curing Reactions to Percolation and Entanglement Analyses. *Polymers* **2025**, *17*.

(39) Penrose, M. D. Connectivity of soft random geometric graphs. *The Annals of Applied Probability* **2016**, *26*, 986–1028.

(40) Saxe, J. B. Embeddability of Weighted Graphs in k-Space is Strongly NP-Hard. Proceedings of the 17th Allerton Conference on Communication, Control, and Computing. 1979; pp 480–489.

(41) Barthélemy, M. Spatial Networks. *Physics Reports* **2011**, *499*, 1–101.

(42) Landrum, G. RDKit: Open-source cheminformatics. 2024; `https://www.rdkit.org`.

(43) Mayo, S. L.; Olafson, B. D.; Goddard, W. A. DREIDING: a generic force field for molecular simulations. *The Journal of Physical Chemistry* **1990**, *94*, 8897–8909.

(44) Kremer, K.; Grest, G. S. Dynamics of entangled linear polymer melts: A molecular-dynamics simulation. *The Journal of Chemical Physics* **1990**, *92*, 5057–5086.

(45) Kong, D.; Yang, M.; Zhang, X.; Du, Z.; Fu, Q.; Gao, X.; Gong, J. Control of Polymer Properties by Entanglement: A Review. *Macromolecular Materials and Engineering* **2021**, *306*, 2100536.

(46) Lee, S.; Huang, Y.; Dai, J.; Kim, H.; Kim, J. Trapping Polymer Entanglements via Prolonged Initiation. *Macromolecules* **2026**, acs.macromol.5c03018.

(47) Lang, M. Elasticity of Phantom Model Networks with Cyclic Defects. *ACS Macro Letters* **2018**, *7*, 536–539.

(48) Lang, M.; Müller, T. On the Reference Size of Chains in a Network and the Shear Modulus of Unentangled Networks Made of Real Chains. *Macromolecules* **2022**, *55*, 8950–8959.

(49) Wang, S.; Ramkrishna, D.; Narsimhan, V. Exact sampling of polymer conformations using Brownian bridges. *Physical Review E* **2020**, *102*, 034901.

(50) Nechaev, S. Concepts of Polymer Statistical Topology. **2017**, 355–388.

(51) Utrera-Barrios, S.; Yu, L.; Skov, A. L. Revisiting the Thermal Transitions of Polydimethylsiloxane (PDMS) Elastomers: Addressing Common Misconceptions with Comprehensive Data. *Macromolecular Materials and Engineering* **2025**, *310*, 2500075.

(52) Zalewski, K.; Chyek, Z.; Trzcinski, W. A. A Review of Polysiloxanes in Terms of Their Application in Explosives. *Polymers* **2021**, *13*, 1080.

(53) Munoz, G.; Dequidt, A.; Martzel, N.; Blaak, R.; Goujon, F.; Devemy, J.; Garruchet, S.; Latour, B.; Munch, E.; Malfreyt, P. Heterogeneity Effects in Highly Cross-Linked Polymer Networks. *Polymers* **2021**, *13*, 757.

(54) Lin, S.; Zhao, X. Fracture of polymer networks with diverse topological defects. *Physical Review E* **2020**, *102*, 052503.

(55) Zhang, Z.; Sachar, H. S. Fracture Behavior of Monodisperse and Polydisperse Polymer Networks: Effects of Topology and Strand-Length Dispersity. *Macromolecules* **2026**, *59*, 99–119.

(56) Zhang, C.; Li, Y.; Wu, Y.; Wang, C.; Liang, J.; Xu, Z.; Zhao, P.; Wang, J. Key Role of Cross-Linking Homogeneity in Polyurethane Mechanical Properties: Insights from Molecular Dynamics. *The Journal of Physical Chemistry B* **2024**, *128*, 12612–12627.

(57) Pournajar, M.; Zaiser, M.; Moretti, P. Edge betweenness centrality as a failure predictor in network models of structurally disordered materials. *Scientific Reports* **2022**, *12*, 15842.

(58) Welch, P.; Welch, C. Eigenvector Centrality is a Metric of Elastomer Modulus, Heterogeneity, and Damage. *Scientific Reports* **2017**, *7*, 818.

(59) Lin, T.-S.; Wang, R.; Johnson, J. A.; Olsen, B. D. Revisiting the Elasticity Theory for Real Gaussian Phantom Networks. *Macromolecules* **2019**, *52*, 1685–1694.

(60) Arora, A.; Lin, T.-S.; Beech, H. K.; Mochigase, H.; Wang, R.; Olsen, B. D. Fracture of Polymer Networks Containing Topological Defects. *Macromolecules* **2020**, *53*, 7346–7355.

(61) Wang, R.; Alexander-Katz, A.; Johnson, J. A.; Olsen, B. D. Universal Cyclic Topology in Polymer Networks. *Physical Review Letters* **2016**, *116*, 188302.

(62) Lutz, J.-F.; Ouchi, M.; Liu, D. R.; Sawamoto, M. Sequence-controlled polymers. *Science* **2013**, *341*, 1238149.

(63) Balazs, A. C.; Emrick, T.; Russell, T. P. Nanoparticle Polymer Composites: Where Two Small Worlds Meet. *Science* **2006**, *314*, 1107–1110.

(64) Moussavi, A.; Wu, Z.; Pal, S.; Keten, S. Nanoconfinement Release Toughens Polymer-Grafted Nanoparticle Assemblies through Better Interdigitation and Entanglements. *Nano Letters* **2025**, *25*.

(65) Rubinstein, M.; Colby, R. H. *Polymer Physics*; Oxford University Press: New York, 2003.

(66) Zhao, X.; Chen, X.; Yuk, H.; Lin, S.; Liu, X.; Parada, G. Soft Materials by Design: Unconventional Polymer Networks Give Extreme Properties. *Chemical Reviews* **2021**, *121*, 4309–4372.

(67) Wang, A.; Sosso, G. C. Graph-based descriptors for condensed matter. *Physical Review E* **2025**, *111*, 064302.

(68) Reyes-Martinez, M. A.; Kadar, A.; Dunne, S.; Glotzer, S. C.; Soles, C. L.; Kotov, N. A. Graph-theoretical description and continuity problems for stress propagation through complex strut lattices. *npj Soft Matter* **2025**, *1*.